IUCrJ
ISSN 2052-2525
BIOLOGY | MEDICINE

Application of differential scanning fluorimetry to X-ray protein crystallography

Yukari Sato[a,b]*‡ and Toshiya Senda[a,c]

[a]Structural Biology Research Center, Institute of Materials Structure and Sciences, High Energy Accelerator Research Organization, 1-1 Oho, Tsukuba, Ibaraki 305-0801, Japan, [b]Graduate School of Life Sciences, Tohoku University, 2-1-1 Katahira, Aoba-ku, Sendai, Miyagi 980-8577, Japan, and [c]Department of Materials Structure Science, School of High Energy Accelerator Science, The Graduate University of Advanced Studies (Soken-dai), 1-1 Oho, Tsukuba, Ibaraki 305-0801, Japan. *Correspondence e-mail: sato.yuka@jihs.go.jp

Received 29 September 2025
Accepted 6 January 2026

Edited by W. Minor, University of Virginia, USA

‡ Present address: Antimicrobial Resistance Research Center, National Institute of Infectious Diseases, Japan Institute for Health Security, 4-2-1 Aobacho, Higashimurayama, Tokyo 189-0002, Japan.

Keywords: protein thermal stability; protein crystallization; improvement of crystal quality; twinning; structure determination; protein structure; X-ray crystallography; crystallization and crystal growth; crystal design.

Supporting information: this article has supporting information at www.iucrj.org

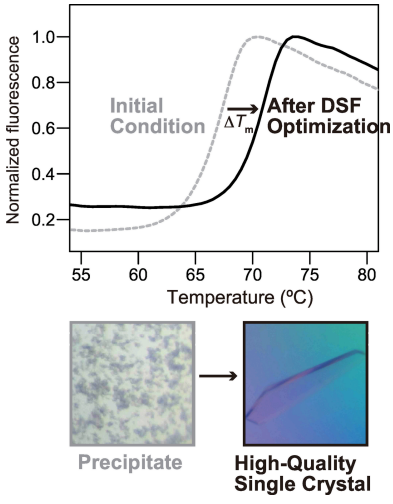

X-ray crystallography remains a powerful technique for determining high-resolution protein structures; however, obtaining high-quality crystals is a significant bottleneck. This study presents a detailed experimental workflow that employs differential scanning fluorimetry (DSF) to optimize protein crystallization. DSF, which measures protein thermal stability, was used to refine both protein buffer composition and crystallization conditions. The method was applied to two distinct proteins: CreD, a nitrosuccinate lyase, and HIRA, a histone chaperone. For CreD, DSF-based optimization of the protein buffer enhanced the crystal quality, increasing the resolution from 3.32 to 2.18 Å. For HIRA(644–1017), DSF-guided optimization of the protein buffer significantly improved the protein solubility from 0.1 to 19.1 mg ml^{-1}, facilitating the growth of initial crystals. Further optimization of the crystallization conditions using DSF, combined with microseeding, improved the crystal quality, leading to structure determination at 2.45 Å resolution. This study demonstrates that DSF is a valuable tool for efficiently optimizing protein crystallization. The workflow presented here, involving initial DSF-based optimization of protein buffers followed by DSF-guided optimization of crystallization conditions, offers a rational approach to enhancing protein crystal quality, thereby facilitating structure determination by X-ray crystallography.

1. Introduction

The number of experimentally determined biological macromolecular structures in the Protein Data Bank (PDB) has increased steadily over the past three decades. While the majority of three-dimensional (3D) structures have been resolved using X-ray crystallography, the number of structures determined by cryogenic electron microscopy (cryo-EM) is growing rapidly (wwPDB Consortium, 2024). Additionally, AI-based structure-prediction programs have emerged and their usage is expanding rapidly. Despite these advancements, X-ray crystallography retains two key advantages: firstly, high-quality crystals enable the determination of atomic positions with sub-ångström precision (Shoemaker & Ando, 2018), and secondly, it allows the use of anomalous scattering to identify specific elements within a structure (Higgins & Lea, 2017; Liu & Hendrickson, 2017). However, obtaining high-quality protein crystals remains a major bottleneck in X-ray crystallography, leading to the proposal of various methods to address the challenges associated with crystallization.

Protein crystallization involves two interdependent steps: nucleation and growth. Both steps require the protein to be in a supersaturated state: a metastable condition where the protein concentration exceeds its solubility limit. Supersaturation is typically induced by adding a precipitant to a

highly concentrated protein solution. Since protein solubility is influenced by multiple factors, including pH, ionic strength and solvent additives, identifying the optimal protein buffer composition to achieve supersaturation for a specific protein can be challenging. Therefore, it is essential to develop effective methods for optimizing both protein and crystallization buffers. Historically, protein crystallographers screened numerous conditions sequentially. The introduction of the sparse-matrix method approximately 30 years ago (Jancarik & Kim, 1991) represented a major breakthrough, greatly enhancing crystallization efficiency. Today, most researchers rely on commercially available crystallization-screening kits. However, when random screening fails to yield high-quality crystals suitable for structure determination, an alternative, preferably physicochemically rational, approach is necessary. Stabilizing the supersaturated state of a protein solution is crucial for successful crystallization, making it essential to establish simple and systematic procedures for evaluating and enhancing protein stability.

Three major methods are widely used to analyze protein stability in solution: differential scanning fluorimetry (DSF), differential static light scattering (DSLS) and dynamic light scattering (DLS) (Pantoliano *et al.*, 2001; Dierks *et al.*, 2008; Vedadi *et al.*, 2010). DSLS and DLS provide physicochemical characterization of proteins without labeling but require specialized instrumentation. In contrast, DSF uses a standard real-time polymerase chain reaction (PCR) instrument, which is widely available in molecular-biology and biochemistry laboratories. DSF assesses thermal stability using a fluorescent dye, such as SYPRO Orange (Epps *et al.*, 2001; Pantoliano *et al.*, 2001; Niesen *et al.*, 2007). The dye binds to hydrophobic regions exposed upon thermal unfolding, causing fluorescence to increase as unfolding progresses. The melting temperature (T_m) of the protein can be estimated from a thermal scan (Poklar *et al.*, 1997). Ligand-bound protein studies show that an increase in T_m correlates with improved protein solubility and ligand-binding affinity, suggesting that a higher T_m often serves as an indicator of protein stabilization by solvent conditions (Vedadi *et al.*, 2006; Niesen *et al.*, 2007). Accordingly, DSF is now widely used. Several studies report DSF-guided buffer optimization for crystallization and 3D structure determination (Ericsson *et al.*, 2006; Philips & de la Peña, 2011; Santos *et al.*, 2012; Vedadi *et al.*, 2006; Ristic *et al.*, 2015; Skagseth *et al.*, 2017; Guo *et al.*, 2018; Sharma & Kumar, 2019). However, detailed rationales for choosing specific buffers and crystallization conditions are rarely reported, posing a challenge to the application of DSF in X-ray crystallography.

In this study, we present an experimental workflow for optimizing protein crystallization conditions using DSF. Using this workflow, we crystallized CreD and histone regulator A (HIRA) by DSF-guided optimization. CreD is a nitrosuccinate lyase in the aspartase/fumarase superfamily of enzymes. It catalyzes nitrous acid elimination in a secondary metabolic pathway of the Gram-positive bacterium *Streptomyces cremeus* (Sugai *et al.*, 2016). Using DSF-guided screening, we obtained high-quality crystals and determined the enzyme structure from the orthorhombic crystals at 2.18 Å resolution (Katsuyama *et al.*, 2018). HIRA is a conserved eukaryotic histone chaperone that mediates incorporation of the histone variant H3.3 into nucleosomes at transcriptionally active regions and DNA-repair sites (Tagami *et al.*, 2004; Ray-Gallet *et al.*, 2011). For the C-terminal half of HIRA (residues 644–1017), hereafter HIRA(644–1017), low solubility after purification was a major obstacle that we mitigated with DSF-guided buffer optimization. Here, we outline the DSF-based procedures used to crystallize these proteins and propose a practical workflow for future crystallization studies.

2. Materials and methods

2.1. Expression and purification of proteins

CreD was overproduced in *Escherichia coli* as described previously (Katsuyama *et al.*, 2018). 6×His-tagged CreD was purified using His60 Ni Superflow Resin (Takara Bio), and the His-tag was cleaved using factor Xa. The protein was further purified by anion-exchange chromatography on a Resource Q column (GE Healthcare) with a linear gradient from buffer *A* [20 m*M* HEPES, 20%(*v*/*v*) glycerol pH 8.0] to buffer *B* [20 m*M* HEPES, 20%(*v*/*v*) glycerol, 1 *M* sodium chloride pH 8.0]. To prevent precipitation of CreD, 20%(*v*/*v*) glycerol was included in all buffers. The tag-free CreD was desalted into buffer *A*. After DSF optimization, the buffer was exchanged for buffer *C* [20 m*M* HEPES, 20%(*v*/*v*) glycerol pH 6.8]. The protein was concentrated using an Amicon Ultra-15 concentrator (Merck), and the concentration was determined by absorbance at 280 nm [$\varepsilon^{280\,\mathrm{nm}}_{\mathrm{CreD}} = 7.4\ \mathrm{cm}^{-1}$ for a 1%(*w*/*v*) solution].

HIRA(644–1017) was overproduced in *E. coli* as described previously (Ray-Gallet *et al.*, 2018) and was purified using the IMPACT system (New England BioLabs) followed by size-exclusion chromatography (SEC). Intein cleavage was performed in either buffer *D* [20 m*M* Tris–HCl pH 8.5, 10%(*v*/*v*) glycerol, 300 m*M* sodium chloride, 50 m*M* DTT] or buffer *E* [20 m*M* Tris–HCl pH 8.5, 10%(*v*/*v*) glycerol, 500 m*M* sodium chloride, 50 m*M* DTT], prepared according to DSF results. HIRA(644–1017) was further purified by SEC on a HiLoad 16/600 Superdex 200 pg column (GE Healthcare) equilibrated with buffer *F* [20 m*M* Tris–HCl pH 8.5, 10%(*v*/*v*) glycerol, 300 m*M* sodium chloride, 2 m*M* DTT], buffer *G* [20 m*M* HEPES–NaOH pH 7.5, 10%(*v*/*v*) glycerol, 300 m*M* sodium chloride, 2 m*M* DTT] or buffer *H* [20 m*M* HEPES–NaOH pH 6.8, 10%(*v*/*v*) glycerol, 500 m*M* sodium chloride, 2 m*M* DTT]. The protein was stored in the final SEC buffer. Protein concentration was determined by absorbance at 280 nm [$\varepsilon^{280\,\mathrm{nm}}_{\mathrm{HIRA(644\text{-}1017)}} = 9.9\ \mathrm{cm}^{-1}$ for a 1%(*w*/*v*) solution]. Selenomethionine (SeMet)-labeled HIRA(644–1017) was overproduced and purified as described previously (Ray-Gallet *et al.*, 2018). SeMet HIRA(644–1017) was purified using the optimized buffers for HIRA(644–1017).

2.2. DSF analysis

A DSF reaction mixture was prepared by combining 2.5 µl 100× SYPRO Orange (Thermo Fisher Scientific) diluted in

protein buffer, 2.5 µl protein solution and 45 µl protein buffer (or 22.5 µl each of buffer *H* and crystallization solution for crystallization assays). CreD and HIRA(644–1017) protein solutions were prepared at 2.0 mg ml^{-1} in buffer *A* and 1.0 mg ml^{-1} in buffer *G*, respectively, for DSF analysis. For the optimization of HIRA(644–1017), 90 crystallization solutions were tested in total, including representative conditions CS-A (0.60 *M* ammonium sulfate, 0.15 *M* sodium citrate pH 5.5), CS-B (0.40 *M* ammonium sulfate, 0.15 *M* sodium citrate pH 5.5) and CS-C (0.60 *M* ammonium sulfate, 0.15 *M* MES–NaOH pH 6.5), as listed in Supplementary Tables S1 and S2.

A 20 µl aliquot of the DSF reaction mixture was transferred into two separate wells (as duplicates) of a 96-well microplate (Bio-Rad, catalogue No. 2239441), centrifuged and then incubated in a MyiQ real-time PCR (RT-PCR) instrument (Bio-Rad). The heat-block temperature was increased from 25°C to 90°C in 0.5°C increments every 10 s. Fluorescence intensity was recorded at each temperature increment. The T_m value was determined as the temperature corresponding to the maximum in the first derivative of the fluorescence signal (Niesen *et al.*, 2007).

2.3. Crystallization

2.3.1. Crystallization of CreD

Initial crystallization screening of CreD was performed manually at 293 K using the sitting-drop vapor-diffusion method with commercially available screening kits: Wizard Classic 1 and 2 (Rigaku) and Index (Hampton Research). The protein concentration was 9.1 mg ml^{-1} in buffer *A*. Crystallization conditions were optimized at 293 K by changing the precipitant concentration and pH. Crystallization droplets were prepared by mixing 1.0–1.4 µl crystallization solution with 4.0 µl 9.1 mg ml^{-1} CreD. In buffer *A*, CreD crystallized in the trigonal form.

Trigonal CreD crystals were cryoprotected using a multistep soaking method (Senda *et al.*, 2016). First, 3–8 µl cryoprotectant solution consisting of 15%(*w*/*v*) maltose, 0.05 *M* bis-Tris pH 6.35–6.40, 12.5%(*v*/*v*) PEG 3350 was added to the crystallization droplets. 3–8 µl of another cryoprotectant solution consisting of 25%(*v*/*v*) DEG, 0.05 *M* bis-Tris pH 6.35–6.40, 12.5%(*w*/*v*) PEG 3350 was then added.

After optimizing the protein buffer using DSF, crystallization screening was repeated at 293 K using additional commercial kits: Crystal Screen (Hampton Research), Crystal Screen 2 (Hampton Research), Stura FootPrint Screen (Molecular Dimensions), MembFac (Hampton Research), Wizard Classic 1 and 2, Protein Complex Suite (Qiagen), PEG/Ion (Hampton Research), PEG/Ion 2 (Hampton Research), Index and PEGs II Suite (Qiagen). The crystallization used an automated protein crystallization and monitoring system (PXS) developed in our laboratory (Hiraki *et al.*, 2006). In this setup, 0.5 µl CreD in buffer *C* (9.8 mg ml^{-1}) was mixed with 0.5 µl crystallization solution. Crystallization conditions were further optimized manually at 293 K using the hanging-drop vapor-diffusion method by adjusting the precipitant concentration and pH. Droplets were prepared by mixing 2 µl 10 mg ml^{-1} protein in buffer *C* with 2 µl crystallization solution. No cryoprotectant solution was used for these crystals.

2.3.2. Crystallization of HIRA(644–1017)

Crystallization screening for HIRA(644–1017) in protein buffers *G* and *H* was performed using PXS (Hiraki *et al.*, 2006) with commercially available kits, including Crystal Screen, Crystal Screen 2, Stura FootPrint Screen, MembFac, Wizard Classic 1 and 2, Protein Complex Suite, PEG/Ion, PEG/Ion 2 and PEGs II Suite.

Manual crystallization was conducted by mixing equal volumes of crystallization and protein solutions. For microseeding, crushed crystals were mixed into droplets prepared by mixing equal volumes of crystallization and protein solutions (Stura & Wilson, 1991; Sato *et al.*, 2007). Cryoprotectant screening was performed using a CryoPro Kit (Hampton Research) and crystals of HIRA(644–1017) were soaked in cryoprotectant solutions and then flash-cooled in liquid nitrogen.

2.4. Diffraction and data collection

Before the X-ray diffraction experiments, all crystals were flash-cooled in liquid nitrogen. Diffraction data sets for CreD and HIRA(644–1017) crystals were collected on beamlines BL15A1 at NSRRC, Taiwan, PF-AR NE3A, BL-1A, BL-5A and BL-17A at the Photon Factory, KEK, Tsukuba, Japan and BL32XU and BL41XU at SPring-8, Harima, Japan. The data sets were processed and scaled using the *XDS* and *XSCALE* programs, respectively (Kabsch, 2010). The highest resolution was defined by the criteria $R_{merge} < 0.5$, completeness > 90% and mean $I/\sigma(I) > 2.4$ in the highest resolution shell.

Diffraction data sets from thin-plate HIRA(644–1017) and SeMet HIRA(644–1017) crystals could not be processed with *XDS*, except for two data sets (one from each protein), owing to poor and anisotropic diffraction. To determine the highest resolution achieved by all mounted HIRA(644–1017) and SeMet HIRA(644–1017) crystals, we used *DISTL* method 2 in the *CCP*4 suite (Zhang *et al.*, 2006).

The *Phenix* suite (Liebschner *et al.*, 2019) and the *CCP*4 suite (Agirre *et al.*, 2023) were used for crystallographic analysis. Molecular graphics were prepared with *PyMOL* (Schrödinger).

3. Results

3.1. Crystallization of CreD

3.1.1. Trigonal crystals of CreD and initial crystallization screening

We evaluated DSF-based buffer screening for protein crystallization using the nitrosuccinate lyase CreD as a case study (Katsuyama *et al.*, 2018; Fig. 1). After purification, CreD was stored and handled in buffer *A*, as established during purification [Fig. 2(*a*)]. Since CreD precipitated in the absence of glycerol, buffer *A* contained 20%(*v*/*v*) glycerol.

Table 1
Data-collection and refinement statistics for CreD.

Values in parentheses are for the highest resolution shell.

	Native	
Data set	Trigonal	Orthorhombic†
X-ray source/beamline	SPring-8/BL41XU	SPring-8/BL41XU
Wavelength (Å)	1.0000	1.0000
Space group	$P3_221$	$I222$
a, b, c (Å)	105.06, 105.06, 189.43	76.81, 98.22, 124.51
α, β, γ (°)	90.00, 90.00, 120.00	90.00, 90.00, 90.00
Resolution (Å)	20.00–3.32 (3.41–3.32)	20.00–2.18 (2.24–2.18)
R_{merge}	0.04 (0.46)	0.07 (0.49)
Completeness (%)	99.5 (100.0)	99.2 (94.6)
Multiplicity	10.49 (10.98)	4.42 (3.16)
Mean $I/\sigma(I)$	34.40 (5.88)	13.63 (2.45)
$CC_{1/2}$ (%)	100.0 (98.1)	99.9 (90.3)
V_M (Å^3 Da^{-1})	3.0	2.3
Solvent content (%)	58.7	47.5

† Data-collection statistics are from Katsuyama *et al.* (2018).

Initial manual screening yielded microcrystals under condition No. 79 of the Index screen [25%(*w*/*v*) PEG 3350, 0.2 *M* ammonium acetate, 0.1 *M* bis-Tris pH 6.5]. To obtain larger crystals, we optimized the conditions by varying the precipitant concentration, protein concentration and pH. Furthermore, we tested additives using the Additive Screen (Hampton Research) and the reaction product of CreD. These optimizations resulted in trigonal crystals [space group $P3_221$, ∼0.30 × 0.20 × 0.20 mm; Fig. 2(*b*)] grown from a solution consisting of 25%(*w*/*v*) PEG 3350, 0.2 *M* ammonium acetate, 0.1 *M* bis-Tris pH 6.4. Diffraction data sets from these crystals reached a resolution of 3.32 Å, and the electron-density map was obtained using molecular replacement (Table 1). However, the map lacked a significant portion of CreD. While CreD is predicted to comprise three domains, D1 (residues 1–105), D2 (residues 106–374) and D3 (residues 375–460), according to the *XtalPred* server (Slabinski *et al.*, 2007), approximately 30% of D2 and 80% of D3 were not visible in the electron-density map [Fig. 2(*c*)]. Although we optimized the cryo-conditions and used multi-step soaking, the diffraction quality did not improve. Because determining the full-length structure of CreD is essential to understand nitrous acid elimination, we sought to improve the crystal quality using DSF-based optimization.

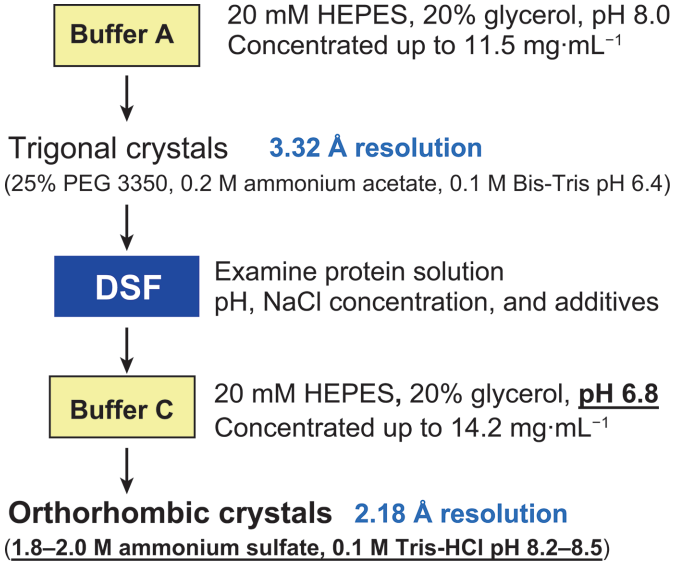

Figure 1
Schematic workflow for DSF-based protein buffer screening in the crystallization of CreD.

3.1.2. Optimization of CreD buffer conditions using DSF

We first optimized the desalting buffer (buffer *A*) using DSF. The effects of pH and sodium chloride concentration were analyzed separately. Among the nine tested pH conditions (ranging from 6.8 to 9.0), 20 m*M* HEPES pH 6.8 yielded the highest T_m value [Fig. 3(*a*)]. Additionally, in the presence of 20 m*M* Tris–HCl pH 7.5 and 10%(*v*/*v*) glycerol, the absence of NaCl produced a higher T_m than the presence of 150 m*M* NaCl [Fig. 3(*b*)].

Next, we examined the effects of additives, including glycerol, DTT and $NaNO_3$, under the optimal pH condition (20 m*M* HEPES pH 6.8). The highest T_m values were observed in buffers containing 20%(*v*/*v*) glycerol, whereas

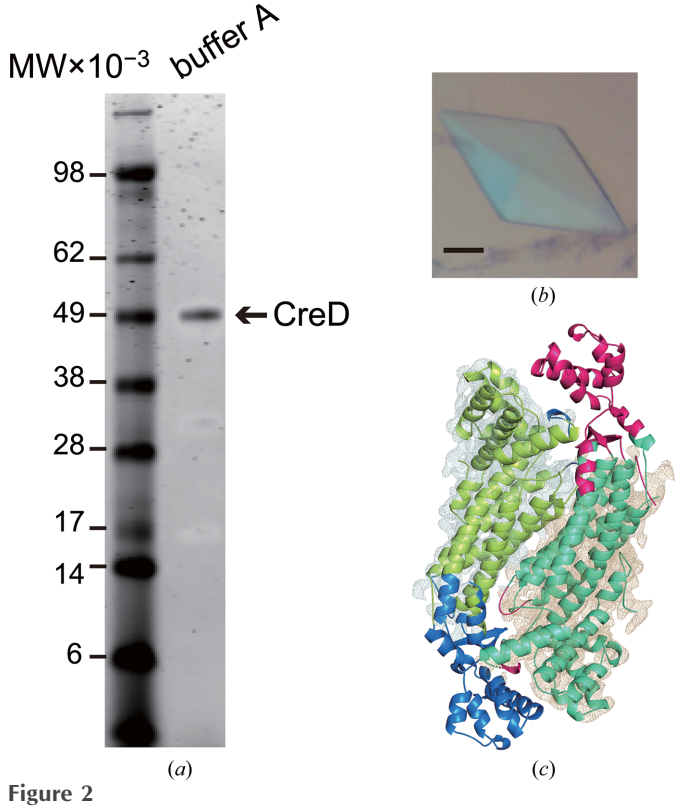

Figure 2
Purification and crystallization of CreD using buffer *A*. (*a*) Representative SDS–PAGE showing CreD in buffer *A*. (*b*) Trigonal CreD crystal. Scale bar: 0.100 mm. (*c*) $2mF_o - DF_c$ electron-density maps of subunits *A* and *F* of the trigonal CreD crystal are shown in light blue and light orange, respectively. The density was contoured at 1σ. A model of the orthorhombic CreD crystal is superimposed. Subunits *A* (x, y, z) and *C* ($x, -y + 1, -z + 2$) of the orthorhombic CreD crystal model are shown in light green and turquoise, respectively. Parts of subunits *A* and *C* of the orthorhombic CreD crystal model that are missing in the trigonal CreD crystal are shown in blue and pink, respectively.

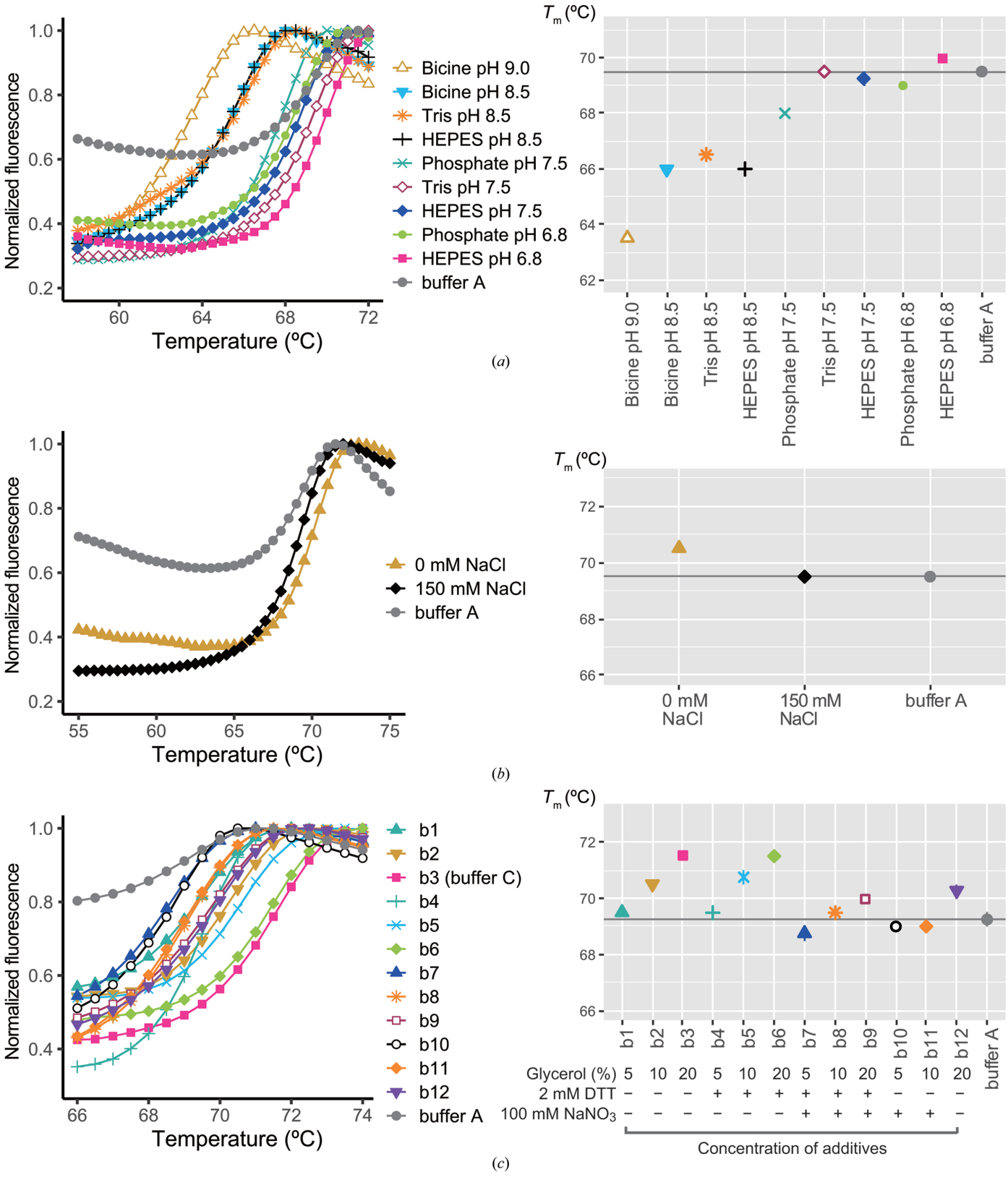

Figure 3
Thermal stability versus pH, ionic strength and additives for CreD: buffer *C* [20 m*M* HEPES, 20%(*v*/*v*) glycerol pH 6.8] yielded the highest thermal stability. Left: thermal denaturation profiles showing normalized fluorescence as a function of temperature. Right: ThermoFluor-derived T_m for CreD varying (*a*) pH in the presence of 150 m*M* NaCl and 10%(*v*/*v*) glycerol, (*b*) NaCl concentration in the presence of 20 m*M* Tris–HCl pH 7.5, 10%(*v*/*v*) glycerol and (*c*) glycerol, DTT and $NaNO_3$ in the presence of 20 m*M* HEPES pH 6.8. Buffer *A* [20 m*M* HEPES, 20%(*v*/*v*) glycerol pH 8.0] was used as the control to assess stability (gray line). The standard deviation of T_m for CreD is indicated by vertical lines in the right panels [visible only for HEPES pH 7.5 in (*a*) and b5, b7, b12 and buffer *A* in (*c*)].

DTT and $NaNO_3$ had no significant effects on the T_m values [Fig. 3(*c*)]. Based on these results, buffer *C* [20 m*M* HEPES, 20%(*v*/*v*) glycerol pH 6.8] was prepared for desalting and storage of CreD.

3.1.3. Crystallization of CreD using the optimized buffer

CreD was concentrated to 9.8 mg ml^{-1} in buffer *C* [Fig. 4(*a*)] and a second round of crystallization screening was performed using the fully automated crystallization system PXS (Hiraki *et al.*, 2006) with commercially available kits. Since we used the automated crystallization screening robot, we could screen more conditions than manual experiments before the DSF optimization. Importantly, while Wizard Classic 1 and 2 were included in both rounds, the results from Wizard Classic 1 and 2 differed before and after optimization. Before optimization, no crystals were obtained from Wizard Classic 1 or 2. By contrast, CreD dissolved in the optimized buffer (buffer *C*) crystallized under condition 3 of Wizard Classic 2 [20%(*w*/*v*) PEG 8000, 0.1 *M* Tris–HCl pH 8.5, 200 m*M* $MgCl_2$] and diffracted to 2.70 Å resolution (Katsuyama *et al.*, 2018).

Furthermore, the crystallization pH shifted from 6.5 in the first round to 8.5 in the second round. Crystallization at pH 8.5 was further confirmed by successful crystallization in condition 4 of Crystal Screen (2.0 *M* ammonium sulfate, 0.1 *M* Tris–HCl pH 8.5). The crystal diffracted to 2.90 Å resolution (Katsuyama *et al.*, 2018). CreD crystallized even at pH 8.0 and below; however, the crystals obtained under these conditions diffracted to 3.20 Å resolution (condition 87 of Protein Complex Suite: 1.6 *M* lithium sulfate, 0.1 *M* Tris pH 8; Katsuyama *et al.*, 2018) or less (Supplementary Table S3).

The crystallization conditions were then optimized by changing the precipitant concentration and pH based on condition 4 of Crystal Screen (pH 8.5), condition 3 of Wizard Classic 2 (pH 8.5) and conditions similar to condition 87 of

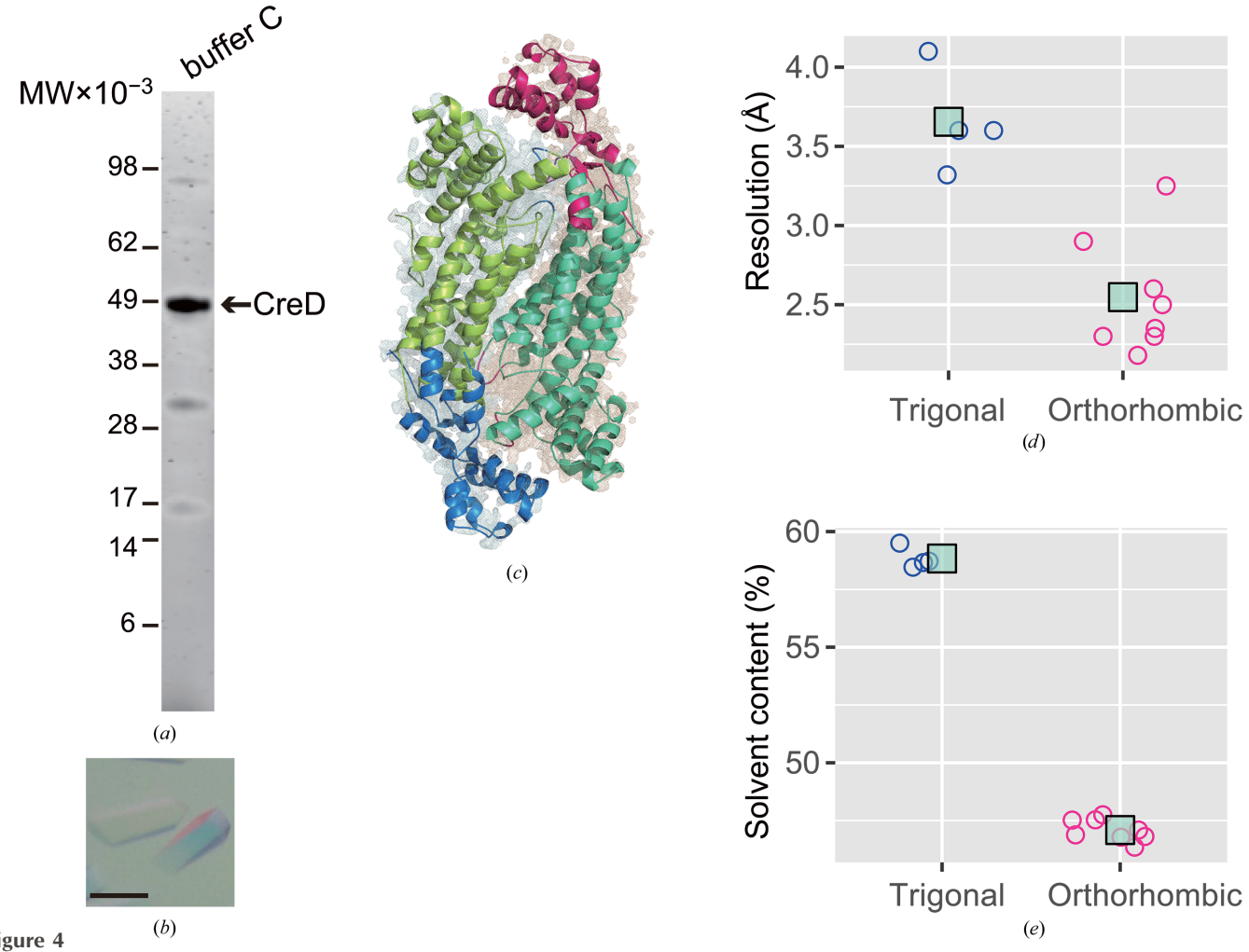

Figure 4
Purification and crystallization of CreD using buffer *C*. (*a*) SDS–PAGE showing CreD in buffer *C*. (*b*) Orthorhombic CreD crystals. Scale bar: 0.100 mm. (*c*) Electron-density maps of the orthorhombic CreD crystal. $2mF_o - DF_c$ electron-density maps of subunits *A* and *C* are shown in light blue and light orange, respectively. The density is contoured at 1σ. (*d*) Resolution of native data for trigonal and orthorhombic crystals collected at a wavelength of 1.0000 Å. The resolution was determined using the *XDS* and *XSCALE* programs (Kabsch, 2010). The turquoise squares represent the mean resolution of CreD crystals. The significance of the difference between the two groups was examined by a two-tailed Wilcoxon rank-sum test: $P = 0.0082$. (*e*) Solvent content for the native data, calculated from the unit cell (Matthews, 1968). The turquoise squares represent the mean solvent content of CreD crystals. The significance of the difference between the two groups was examined by a two-tailed Wilcoxon rank-sum test: $P = 0.0040$.

Protein Complex Suite (pH 8) (Katsuyama *et al.*, 2018). These efforts yielded orthorhombic crystals in a solution consisting of 0.1 *M* Tris–HCl pH 8.2–8.5, 1.8–2.0 *M* ammonium sulfate [Fig. 4(*b*); Table 1]. These crystals belonged to space group *I*222 and their structure was determined at 2.18 Å resolution (Table 1; PDB entry 5xny), allowing modeling of 92% of D2 and 95% of D3 [Fig. 4(*c*)]. The resolution of the newly obtained crystals was significantly improved compared with the original trigonal crystals, and the solvent content (Matthews, 1968) was reduced [Figs. 4(*d*) and 4(*e*)]. We examined two cryoprotectants; no improvement of the crystal quality was observed in the orthorhombic crystal.

3.2. Crystallization of HIRA(644–1017)

3.2.1. Initial screening of protein buffer and crystallization conditions for HIRA(644–1017)

We also applied DSF to a broader optimization strategy that included both protein buffer and crystallization buffers. This approach allowed us to determine the crystal structure of HIRA(644–1017) at 2.45 Å resolution (Fig. 5).

HIRA(644–1017) was purified using the IMPACT system (New England BioLabs), which utilizes intein cleavage. The intein cleavage required DTT and alkaline pH in a reaction buffer (buffer *D*; Chong *et al.*, 1996). After cleavage, HIRA(644–1017) was further purified by gel filtration in SEC buffer (buffer *F*) [Fig. 6(*a*)], which was prepared based on the reaction buffer used during cleavage. Although HIRA(644–1017) was successfully purified in this way [Fig. 6(*b*)], the purified protein formed granular precipitates immediately after gel filtration [Fig. 6(*c*)] and could not be concentrated above 0.1 mg ml^{-1}.

To improve protein solubility, we changed the pH of the SEC buffer from 8.5 to 7.5 (buffer *G*), allowing HIRA(644–1017) to be concentrated to 1.2 mg ml^{-1} without precipitation [Fig. 6(*d*)]. However, no crystals were obtained during screening. Since the concentration (1.2 mg ml^{-1}) was still relatively low for crystallization, we applied DSF to further improve the solubility.

3.2.2. Optimization of HIRA(644–1017) buffer using DSF

We first optimized the pH and the NaCl concentration separately, as in the DSF analysis of CreD [Figs. 7(*a*) and 7(*b*)]. Nine pH conditions were tested using Bicine–NaOH, HEPES–NaOH, potassium phosphate or Tris–HCl buffer in the presence of 150 m*M* NaCl and 10%(*v*/*v*) glycerol. The highest T_m value was observed with 20 m*M* HEPES–NaOH pH 6.8

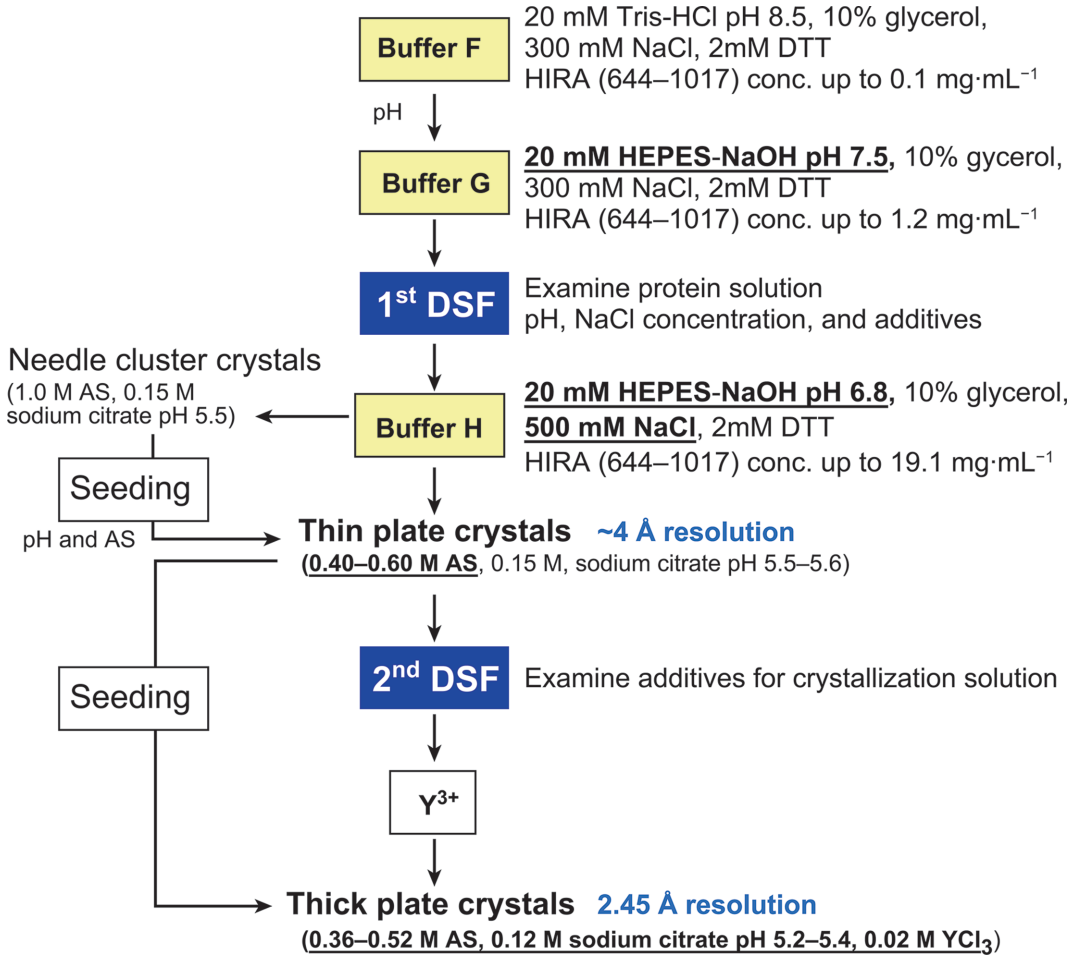

Figure 5
Schematic workflow for DSF-based protein buffer and crystallization solution screening for the crystallization of HIRA(644–1017). AS, ammonium sulfate.

[Fig. 7(*a*)]. Next, we evaluated five NaCl concentrations in 20 m*M* Tris–HCl pH 7.5; the highest T_m value was obtained at 500 m*M* NaCl [Fig. 7(*b*)].

We also examined the effects of $NaNO_3$ and $MgCl_2$ on protein stability using SEC buffer (buffer *G*) but observed no improvements [Fig. 7(*c*)]. Next, we analyzed the effects of additives, including DTT and glycerol, in the presence of 20 m*M* HEPES–NaOH pH 6.8 and 500 m*M* NaCl. The highest T_m value was observed with 10% glycerol and 0.5 or 2 m*M* DTT [Fig. 7(*d*)]. Based on these results, we formulated a new SEC buffer [buffer *H*; 20 m*M* HEPES–NaOH pH 6.8, 10%(*v*/*v*) glycerol, 500 m*M* sodium chloride, 2 m*M* DTT]. However, since pH affects the efficiency of tag cleavage in the IMPACT system (Chong *et al.*, 1996), the new SEC buffer (pH 6.8) was unsuitable for intein cleavage, because efficient cleavage requires an alkaline pH of around 8.0. Therefore, we prepared a new reaction buffer (pH 8.5) for intein cleavage based on the DSF results. To stabilize HIRA(644–1017) during cleavage, we optimized the NaCl concentration for the new reaction buffer (buffer *E*) using DSF results.

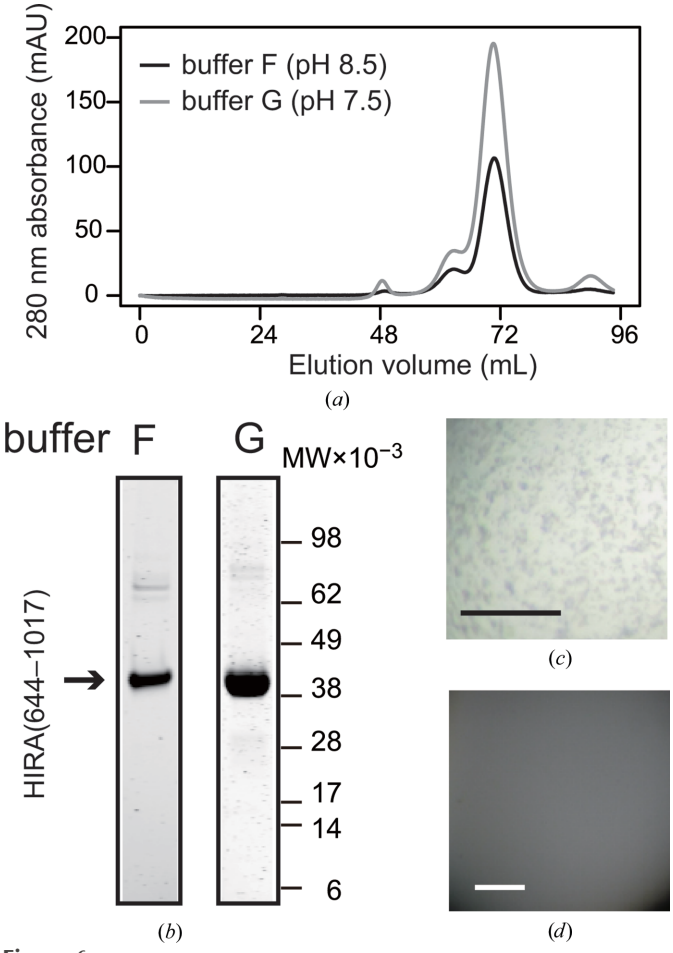

Figure 6
Purification of HIRA(644–1017) using buffer *F* or *G*. (*a*) HiLoad 16/600 Superdex 200 pg chromatograms of HIRA(644–1017). (*b*) SDS–PAGE showing HIRA(644–1017). (*c*) HIRA(644–1017) precipitated in buffer *F* at concentrations higher than 0.1 mg ml^{-1}. (*d*) HIRA(644–1017) remained soluble in buffer *G* at 1.2 mg ml^{-1}. Scale bar: 0.010 mm.

3.2.3. Effects of buffers *E* and *H* on HIRA(644–1017) purification

We tested the new cleavage and SEC buffers (buffers *E* and *H*) for protein purification. Tag cleavage with intein was successful in buffer *E*. Notably, although HIRA(644–1017) precipitated within one day when the cleavage reaction was conducted in buffer *D* (Fig. 8), buffer *E* prevented precipitation and maintained HIRA(644–1017) in soluble form for up to three days after cleavage at 4°C (Fig. 8). Furthermore, SEC purification of HIRA(644–1017) with the new SEC buffer (buffer *H*) resulted in a 2.8-fold increase in protein yield compared with that obtained with buffer *F*. After purification, HIRA(644–1017) was successfully concentrated to 19.1 mg ml^{-1} (Ray-Gallet *et al.*, 2018). Stabilizing HIRA(644–1017) in the new SEC buffer significantly improved protein purification and handling.

3.2.4. Crystallization screening of HIRA(644–1017) purified with the new buffers

Crystallization screening of HIRA(644–1017) purified with the new buffers was performed using PXS with nine commercially available screening kits (Crystal Screen, Crystal Screen 2, Stura FootPrint Screen, MembFac, Wizard Classic 1 and 2, Protein Complex Suite, PEG/Ion and PEG/Ion 2). We tested two protein concentrations (3.1 and 12.2 mg ml^{-1}) and obtained needle cluster crystals of HIRA(644–1017) at 12.2 mg ml^{-1} [Fig. 9(*a*)] under crystallization conditions consisting of 0.15 *M* sodium citrate, 1.0 *M* ammonium sulfate pH 5.5 (condition No. 14 of the Stura FootPrint screen).

Since the resulting crystals were too thin for crystallographic analysis, we applied microseeding to improve their quality. We prepared 81 crystallization solutions by varying the precipitant concentration and pH of the conditions that produced the needle cluster crystals (Supplementary Table S1). Crystallization experiments using 11.2–19.1 mg ml^{-1} HIRA(644–1017) and the prepared solutions produced thin plate crystals under conditions consisting of 0.40–0.60 *M* ammonium sulfate, 0.15 *M* sodium citrate pH 5.5–5.6. The crystals were large enough for crystallographic analysis [0.001 × 0.125 × 0.075 mm; Fig. 9(*a*)] and belonged to the monoclinic space group *C*2 (hereafter referred to as thin plate crystals). While some thin plate crystals diffracted to 4.00 Å resolution (Table 2), the *L*-test revealed pseudo-merohedral twinning with a twin fraction of 0.358 (Padilla & Yeates, 2003; Evans, 2011). For better crystallographic analysis, a higher resolution crystal without twinning was required.

3.2.5. DSF-guided optimization of crystallization conditions for HIRA(644–1017)

To overcome these limitations, we optimized the crystallization conditions using DSF. First, we examined the effects of pH and precipitant concentration using three crystallization solutions: CS-A, CS-B and CS-C. DSF analysis revealed equally high T_m values for CS-A (0.60 *M* ammonium sulfate and pH 5.5) and CS-B (0.40 *M* ammonium sulfate and pH 5.5), whereas CS-C (0.60 *M* ammonium sulfate and pH 6.5)

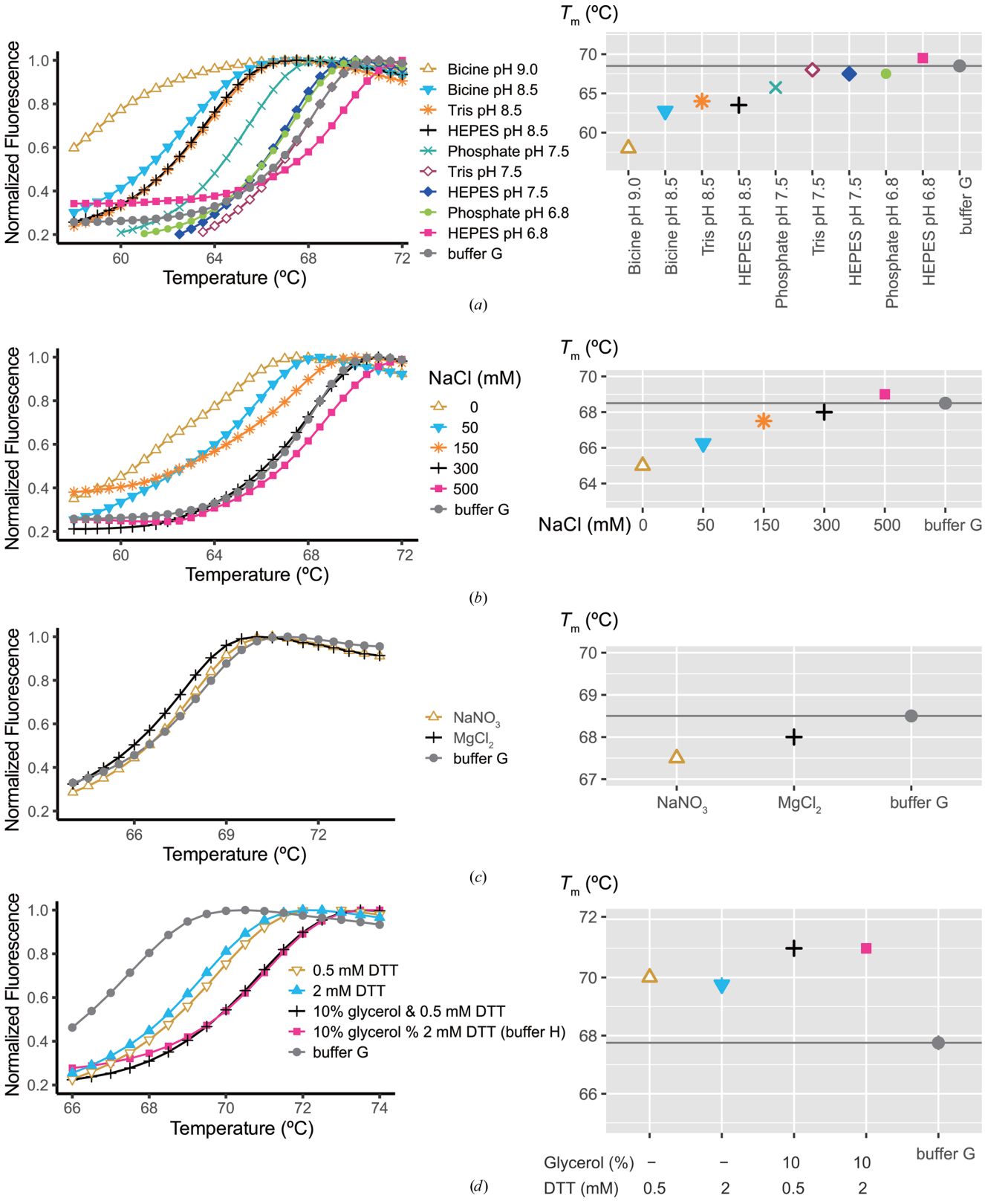

Figure 7
Thermal stability versus pH, ionic strength and additives for HIRA(644–1017): buffer *H* [20 m*M* HEPES–NaOH pH 6.8, 10%(*v*/*v*) glycerol, 500 m*M* NaCl, 2 m*M* DTT] yielded the highest thermal stability. Variation of (*a*) pH values in the presence of 10%(*v*/*v*) glycerol and 150 m*M* NaCl, (*b*) NaCl concentration in the presence of 20 m*M* Tris–HCl pH 7.5, (*c*) $NaNO_3$ or $MgCl_2$ in the presence of 20 m*M* Tris–HCl pH 7.5, 10%(*v*/*v*) glycerol, 300 m*M* NaCl, 2 m*M* DTT and (*d*) DTT and glycerol concentrations in the presence of 20 m*M* HEPES–NaOH pH 6.8 and 500 m*M* NaCl. Buffer *G* [20 m*M* HEPES–NaOH pH 7.5, 10%(*v*/*v*) glycerol, 300 m*M* NaCl, 2 m*M* DTT] was used as the control to assess stability (gray line). The standard deviation of T_m is indicated by vertical lines in the right panels [visible only for 2 m*M* DTT and buffer *G* in (*d*)].

Table 2
Data-collection statistics for HIRA(644–1017).

Values in parentheses are for the highest resolution shell. ND, not determined.

	Native SAD	Native		Se-SAD	
Data set	Thin plate	Thin plate	Thick plate†	Thin plate	Thick plate†
X-ray source/beamline	PF/BL-1A	PF/BL-17A	PF/BL-17A	PF/BL-17A	SPring-8/BL41XU
Wavelength (Å)	2.700	0.9800	0.9800	0.9790	0.9790
Space group	*C*2	ND	*C*2	*C*2	*C*2
a, *b*, *c* (Å)	149.61, 86.94, 211.90	ND	149.99, 86.80, 99.15	152.21, 87.80, 198.84	149.41, 86.85, 98.11
α, β, γ (°)	90.00, 110.45, 90.00	ND	90.00, 102.49, 90.00	90.00, 93.90, 90.00	90.00, 101.67, 90.00
Resolution (Å)	50.00–4.00 (4.10–4.00)	6.98‡	20.00–2.45 (2.51–2.45)	20.00–8.10 (8.32–8.10)	20.00–2.55 (2.62–2.55)
R_{merge}	0.18 (0.28)	ND	0.04 (0.50)	0.27 (0.39)	0.05 (0.46)
Completeness (%)	95.8 (93.2)	ND	99.5 (99.8)	91.7 (99.2)	98.3 (99.0)
Multiplicity	1.77 (1.69)	ND	3.48 (3.50)	3.02 (3.15)	3.55 (3.62)
Mean $I/\sigma(I)$	3.67 (2.47)	ND	19.40 (2.86)	3.39 (2.57)	14.97 (2.88)
$CC_{1/2}$ (%)	89.7 (81.0)	ND	99.9 (82.0)	87.6 (81.2)	99.8 (88.5)
V_M (Å^3 Da^{-1})	2.6	ND	2.5	2.6	2.5
Solvent content (%)	52.1	ND	50.9	53.3	50.4

† The data-collection statistics are from Ray-Gallet *et al.* (2018). ‡ The resolution was assessed with method 2 in the *DISTL* program (Zhang *et al.*, 2006).

exhibited a lower T_m [Fig. 9(*b*), top]. These results suggested that 0.40–0.60 *M* ammonium sulfate had little effect on crystal quality and that pH 6.5 was unsuitable for crystallization. Consistent with DSF predictions, HIRA(644–1017) crystallized in CS-A and CS-B but failed to crystallize in CS-C [Fig. 9(*a*)].

Next, we analyzed the effects of additives using the Additive Screen (Hampton Research). A total of 81 crystallization solutions based on CS-B were tested with various additives [Fig. 9(*b*); Supplementary Table S2]. Increased T_m values were observed for six additives, including potassium chloride (CS16) from the monovalent anion and cation group, potassium sodium tartrate (CS22) from the divalent anion group, and xylitol (CS56), sorbitol (CS57), trehalose (CS59) and glycerol (CS62) from the polyol group [Fig. 9(*b*), top]. Since monovalent anions and cations, divalent anions and polyols were already present in CS-B and/or the protein buffer (buffer *H*) and are commonly used as cryoprotectants, these additives were expected to have a minimal impact on crystallization. Indeed, these polyols were used in a screen of cryoprotectants but did not improve crystal quality (Supplementary Table S4). We instead focused on trivalent cations [yttrium(III) chloride (CS9), chromium(III) chloride (CS13) and praseodymium(III) acetate (CS14)] because more than half of the trivalent cations showed an equal T_m to CS-B [Fig. 9(*a*), top] and multivalent ions are known as the most efficient precipitants (McPherson & Gavira, 2014). In addition, we tested volatile organic compound reagents with equal T_m values to CS-B because they had not been well tested previously.

Crystallization with ethyl acetate and acetone resulted in only thin plate crystals and precipitate, respectively [Fig. 9(*a*)], suggesting that they were ineffective in improving crystal quality. In contrast, crystallization with yttrium(III) chloride produced thick plate-like crystals from a solution consisting of 0.36–0.52 *M* ammonium sulfate, 0.12 *M* sodium citrate pH 5.2–5.4, 0.02 *M* yttrium(III) chloride [Fig. 9(*a*); hereafter referred to as thick plate crystals]. Yttrium(III) chloride was also effective for selenomethionine (SeMet)-labeled HIRA(644–1017). The resolution of the newly obtained thick plate crystals was significantly improved compared with the original thin plate crystals [Fig. 9(*c*)]. The space group of the thick plate crystals was monoclinic *C*2. The unit-cell parameters of the *C*2 cell did not meet the conditions for pseudo-merohedral twinning (Table 2; Parsons, 2003; Nevskaya *et al.*, 2005; Hamdane *et al.*, 2009). Using these crystals, we determined the crystal structure of HIRA(644–1017) at 2.45 Å resolution (Ray-Gallet *et al.*, 2018).

3.2.6. Sulfate ions providing packing interactions

A T_m shift in DSF reflects solvent-induced stabilization of proteins (Vedadi *et al.*, 2010). Protein stability depends on general solution components such as buffers, salts and detergents, the interactions of which with proteins may be specific or nonspecific (Vedadi *et al.*, 2006). Here, we specifically addressed how crystallization solution components, which putatively stabilized the proteins, were positioned in the crystals. Three sulfate ions (S1, S2 and S3) were identified in a HIRA(644–1017) trimer, which comprises subunits *A*, *B* and *C*

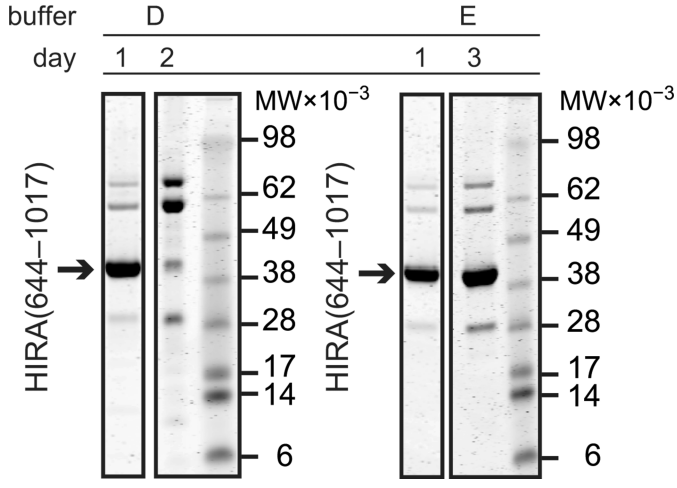

Figure 8
HIRA(644–1017) precipitated after one day of tag-cleavage reaction in buffer *D* [20 m*M* Tris–HCl pH 8.5, 10%(*v*/*v*) glycerol, 50 m*M* DTT, 300 m*M* NaCl] and was soluble in buffer *E* [20 m*M* Tris–HCl pH 8.5, 10%(*v*/*v*) glycerol, 50 m*M* DTT, 500 m*M* NaCl] for three days.

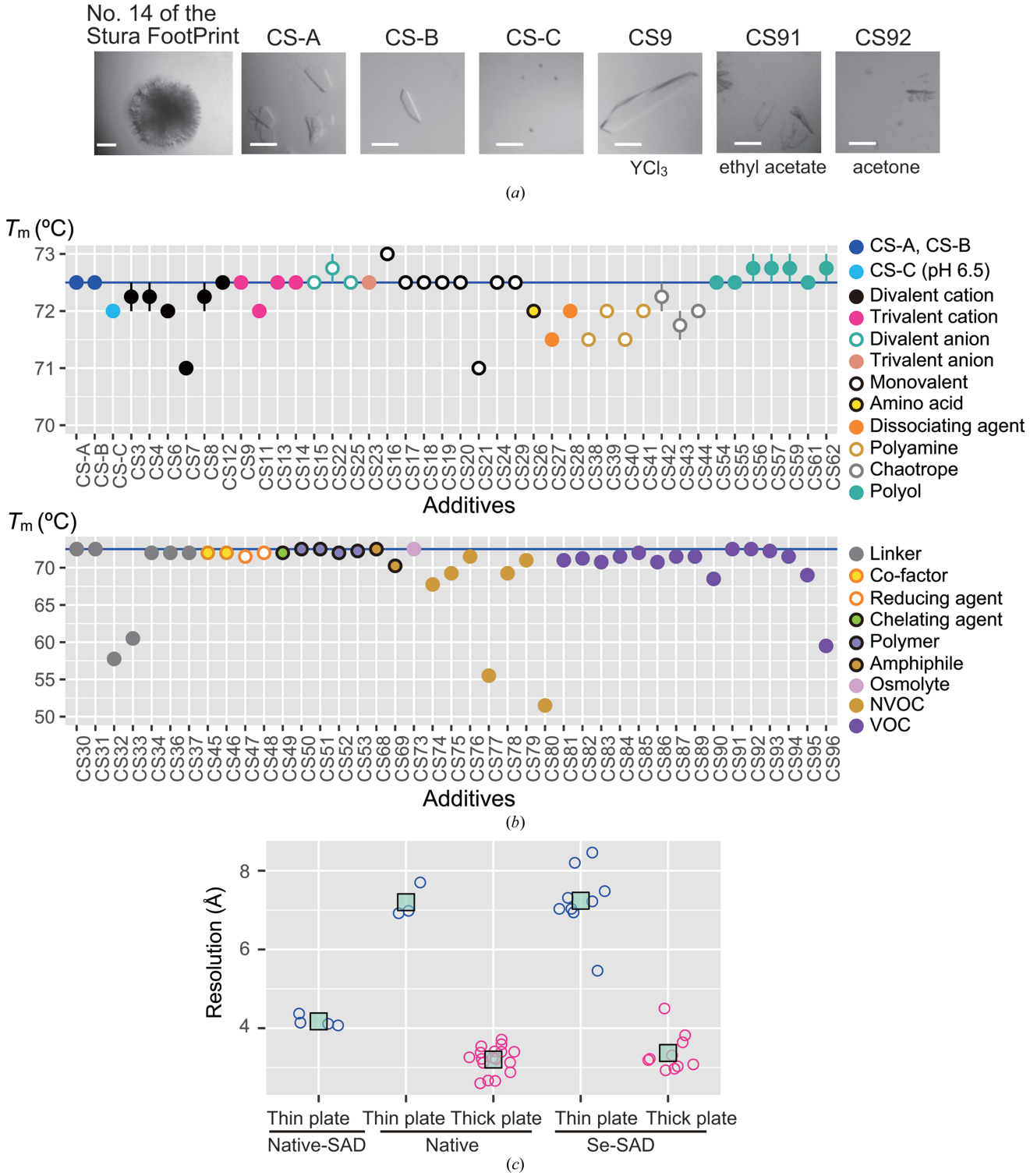

Figure 9
Application of DSF to improve the diffraction quality of HIRA(644–1017) crystals. (*a*) Photographs of representative crystals. Needle cluster crystals appeared under condition No. 14 of the Stura FootPrint screen. Thin plate crystals formed after seeding with CS-A (0.60 *M* ammonium sulfate, 0.15 *M* sodium citrate pH 5.5) or CS-B (0.40 *M* ammonium sulfate, 0.15 *M* sodium citrate pH 5.5), but did not appear after seeding with CS-C (0.60 *M* ammonium sulfate, 0.15 *M* MES–NaOH pH 6.5). The thick plate crystal was obtained in the presence of YCl_3, and crystals resembling thin plates were obtained in the presence of ethyl acetate or acetone. Scale bar: 0.100 mm. (*b*) ThermoFluor-derived T_m for HIRA(644–1017) with variation in pH, precipitant concentration and additives. CS-B was used as the control to assess stability (blue line). The standard deviation of T_m is indicated by vertical lines (visible only for CS3, CS4, CS8, CS22, CS42, CS43, CS56, CS57, CS59 and CS62). Details of the additives are provided in Supplementary Table S2. (*c*) Resolution of the native SAD, native and Se-SAD data collected at wavelengths of 2.7000, 0.9790–1.0000 and 0.9784–0.9790 Å, respectively. The resolution was determined using method 2 in the *DISTL* program (Zhang *et al.*, 2006). The turquoise squares indicate the mean resolution. The significance of the difference between the two groups was examined by a two-tailed Wilcoxon rank-sum test: $P = 0.0077$ for native and $P = 0.0003$ for Se-SAD.

within the asymmetric unit of thick plate crystals [Fig. 10(*a*); PDB entry 5yje; Ray-Gallet *et al.* (2018)]. S1 in subunit *A* interacts with His832 and Ser932 in the same subunit [Fig. 10(*b*)]. Conversely, S2 and S3 mediate crystal packing by interacting with trimers in adjacent asymmetric units. S2 is located at the center of three HIRA(644–1017) trimers, interacting with main-chain amide groups of His908 in subunits *B*, *A* and *C* of three distinct HIRA trimers. In addition, S2 forms hydrogen bonds to three water molecules [Fig. 10(*c*)]. S3 (subunit *C*) interacts with Leu903, Phe904 and Ser905 of subunit *C* and Arg720 of subunit *A* of an adjacent HIRA(644–1017) trimer in the crystal lattice [Fig. 10(*d*)].

4. Discussion

We obtained high-quality crystals using DSF for two distinct proteins: CreD and HIRA(644–1017). The resolution of the diffraction from the CreD crystal was improved from 3.32 to 2.18 Å solely by optimizing the protein buffer. The crystal structure of HIRA(644–1017) was likewise obtained through DSF-based optimization. Optimization of the HIRA(644–1017) protein buffer allowed concentration of the protein solution to 19.1 mg ml^{-1}, whereas it initially precipitated at only 0.1 mg ml^{-1}. Subsequently, the combination of DSF-based optimization of crystallization solutions and micro-seeding improved the crystal quality and enabled structure determination to 2.45 Å resolution.

Protein stability and solubility are important not only for crystallization but also for a wide range of biochemical studies. Unstable protein solutions frequently cause poor reproducibility in such experiments. In many cases, however, protein buffer conditions are chosen empirically. As shown in the example of CreD, optimization of the protein buffer can improve the crystal quality. In the case of HIRA(644–1017), protein buffer optimization facilitated protein solution handling and increased the yield of protein purification. Therefore, it is highly recommended that protein buffer conditions be optimized before starting biochemical experiments, including crystallization screening. The optimization of the protein buffer should be performed in three steps. Firstly, to accurately measure the T_m value, it is necessary to determine the appropriate protein concentration for DSF (Vedadi *et al.*, 2006). Secondly, the protein buffer conditions should be optimized with respect to buffer composition, pH and salt (*e.g.* NaCl) concentration. Finally, an appropriate additive should be identified using DSF in the optimized protein buffer from the second step.

Crystal pathologies are common problems in protein crystallography (Thompson, 2017). In the case of crystal disorder, which causes poor resolution, anisotropic diffraction and so on, several methods have been proposed to address these problems (Yeates & Fam, 1999; Dauter, 2003). One of the most widely used methods is dehydration (Heras *et al.*, 2003). Humidity control is also used via specialized devices (Kiefer-

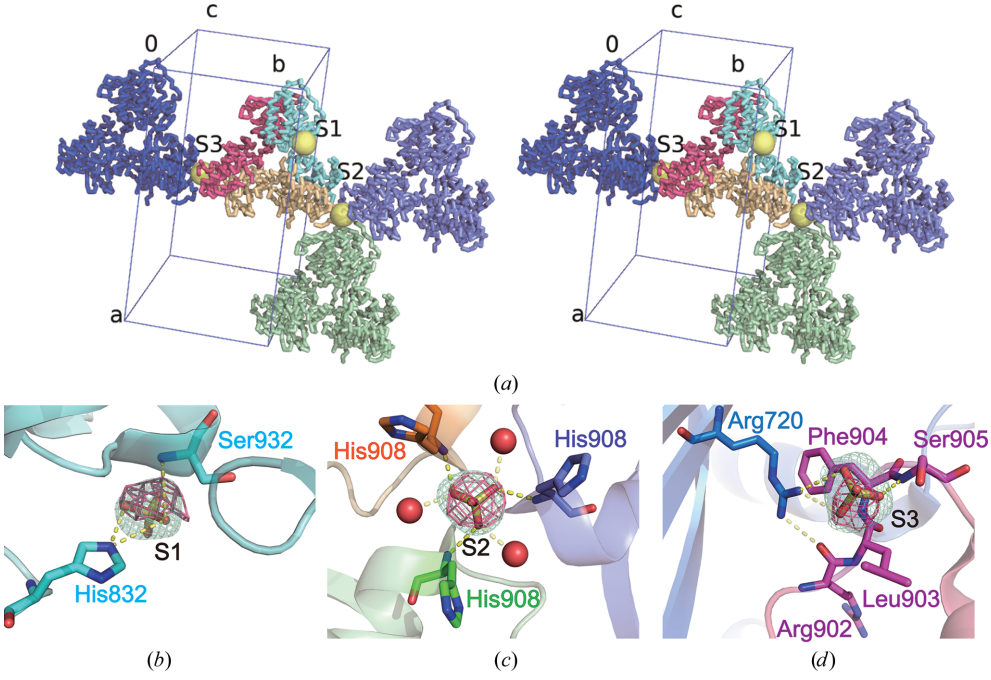

Figure 10
Sulfate ion binding contributes to the crystal packing of HIRA(644–1017). (*a*) Stereo view of the crystal packing around the asymmetric unit trimer. Subunits *A*, *B* and *C* of the asymmetric unit trimer are shown in cyan, light orange and magenta, respectively. Three adjacent crystallographic symmetry-related trimers sym1 ($x + 1/2, y - 1/2, z$), sym2 ($x, y - 1, z$) and sym3 ($x, y + 1, z$) are shown in light green, light blue and blue, respectively. Three sulfate ions, S1, S2 and S3, are shown as yellow spheres. (*b*) S1 (subunit *A*) interacts with His832 and Ser932 in the same subunit. (*c*) S2 (subunit *B*) interacts with three His908 residues (subunit *B*, subunit *A* of sym1 and subunit *C* of sym2) and three water molecules (subunit *B*). Water molecules are shown as red spheres. (*d*) S3 (subunit *C*) interacts with Leu903 (subunit *C*), Phe904 (subunit *C*), Ser905 (subunit *C*) and Arg720 (subunit *A* of sym3). Arg720 (subunit *A* of sym3) interacts with Arg902 (subunit *C*). The $mF_o - DF_c$ simulated-annealing (SA) omit map and the anomalous difference Fourier map of phasing data (Ray-Gallet *et al.*, 2018) for each sulfate ion are shown in pale cyan and pink, respectively. The density is contoured at 3σ.

sauer *et al.*, 2000). We have also proposed a method to improve crystal quality after obtaining crystals (post-crystallization treatment); optimization of the cryo-conditions can improve crystal quality in many cases (Senda *et al.*, 2008; Senda & Senda, 2016; Senda *et al.*, 2016). These methods can modulate crystal packing and reduce disorder within the crystal lattice. However, in the case of CreD, neither optimization of cryoconditions nor dehydration improved the crystal quality. Only optimization of the protein buffer improved the crystal quality. This suggests that crystal lattices sometimes cannot be modulated by post-crystallization treatments. In such cases, modulation of intermolecular interactions may be required before crystallization. Therefore, changing the protein buffer, especially DSF-based optimization of protein buffer and crystallization solution, is effective.

Of the crystal pathologies, macroscopic and intrinsic twinning problems are rarely overcome by post-crystallization treatments. To address macroscopic and intrinsic twinning, modulating intermolecular interactions during crystal growth appears to be effective. We have reported that the seeding method can eliminate macroscopic twinning (Sato *et al.*, 2007) and merohedral twinning (Harada *et al.*, 2016), even when crushed twinned crystals were used as seeds. Our present results show that optimization of the protein buffer and crystallization solution using DSF can eliminate pseudo-merohedral twinning in combination with the seeding method. This suggests that modulating protein environments in solution can change intermolecular interactions, enabling the elimination of crystal twinning. Indeed, two studies on bacteriorhodopsin and on Δ1-pyrroline-5-carboxylate dehydrogenase demonstrated that twinning was avoided by reducing the salt concentration in crystallization or removing lithium chloride from the crystallization solution (Efremov *et al.*, 2004; Inagaki *et al.*, 2005). Therefore, protein buffers and crystallization solutions should be optimized in advance to achieve the minimum required composition before performing additive screening. In the HIRA(644–1017) crystal, sulfate ions appeared to assist in the packing of individual asymmetric units; however, those ions were also included in the crystallization solution for thin plate crystals. Thus, fine tuning of crystallization solutions based on DSF findings was critical in our study.

In conclusion, DSF-based buffer optimization proves effective for increasing protein stability, thereby enhancing both protein purification and subsequent crystallization success. Furthermore, by modulating intermolecular interactions, buffer optimization using DSF can also be employed to mitigate issues such as pathological crystals, which include phenomena such as crystal disorder and twinning. Given the critical role of protein stability in protein experiments, we broadly recommend DSF for studies in biochemistry and biophysical chemistry. Enhanced protein stability and solubility could also expand the range of physicochemical experiments, including techniques such as solution NMR. Based on the current results, it is reasonable to optimize buffer conditions before initiating crystallization screening, potentially incorporating this step as a standard part of the purification procedure, as demonstrated with HIRA. Such proactive optimization can significantly reduce the difficulties encountered during initial crystallization screenings.

However, even after optimizing the protein storage buffer, achieving high crystal quality frequently requires further optimization of the crystallization solution, such as the strategic use of additives. Based on these findings, we propose a general protocol for crystallization guided by DSF [Fig. 11(*a*)]. DSF optimization can be performed at virtually every step of the crystallization process, from initial protein solution concentration to the refinement of the final crystallization conditions, including the selection of effective additives. In DSF-based optimization, parameters often need to be optimized sequentially; when multiple parameters require

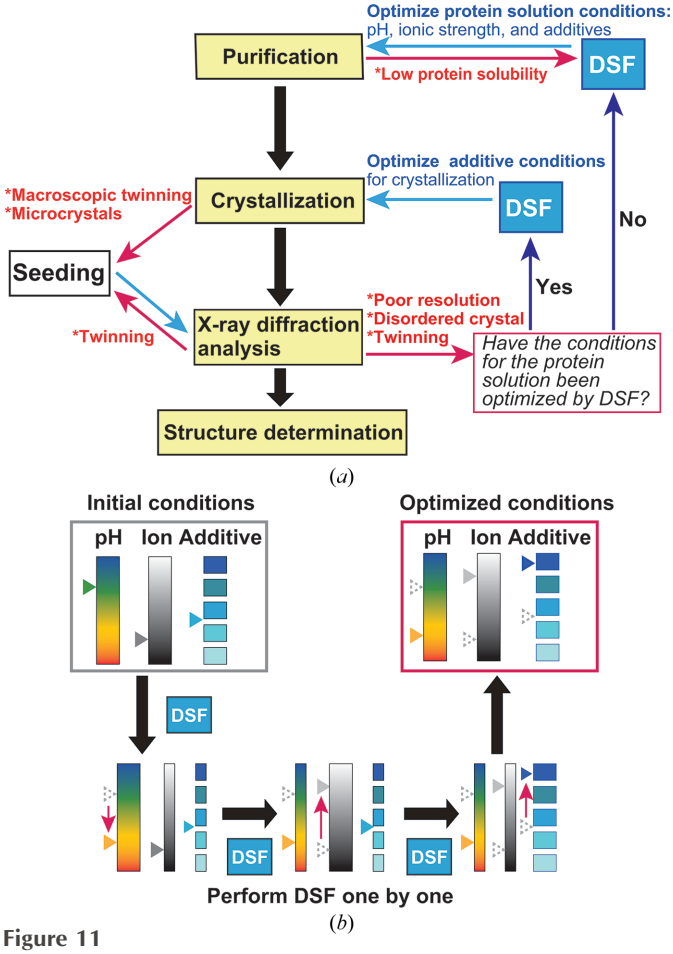

Figure 11
A general protocol for crystal structure determination guided by DSF. (*a*) DSF optimization can be applied at multiple steps throughout the X-ray crystallographic analysis workflow. The blue boxes and arrows indicate steps where DSF is used to optimize conditions, such as the protein solution (pH, ionic strength and additives) during purification and the additive conditions for crystallization. The red arrows and text highlight common problems encountered at each stage of the X-ray crystallographic analysis (*e.g.* low protein solubility, twinning, disordered crystal). Applying DSF can help mitigate these issues. (*b*) Strategy for sequential parameter optimization using DSF. When multiple parameters (*e.g.* pH, ion concentration and specific additives) require optimization, they can be effectively optimized in a step-by-step, sequential manner, as illustrated.

adjustment, we demonstrated that a step-by-step, sequential optimization method can be highly effective [Fig. 11(*b*)].

Furthermore, combining DSF buffer optimization with automated screening robots would effectively improve crystallization success rates, as crystallization experiments remain inherently empirical even after protein buffer optimization. We anticipate that accumulating a vast number of optimization examples through robotics will contribute to establishing protocols for automated protein crystallization and crystal quality improvement, paving the way for future AI-driven automation.

Acknowledgements

The synchrotron-radiation experiments were performed with the approval of the Japan Synchrotron Radiation Research Institute (JASRI; proposal Nos. 2015B1049 and 2016A2749) and the Photon Factory Program Advisory Committee (proposal No. 2015G122). We thank Yohei Katsuyama, Yousuke Higashiyama, Yoshinori Sugai, Miki Senda and Yasuo Ohnishi for help with the crystallization of CreD. YS thanks Cindy Benod for technical help with DSF data analysis, Naoyuki Kuwabara and Hisayoshi Makyio for data collection from the thin plate crystals of HIRA(644–1017) at BL-15A1 and BL32XU, Nobuhiro Suzuki for discussions regarding the anomalous difference Fourier map, Hirokazu Yano for *R* scripts and Tomoya Ota for technical assistance.

Conflict of interest

No conflicts of interest are declared.

Funding information

The following funding is acknowledged: Japan Society for the Promotion of Science (grant No. 16K14908 to Yukari Sato; grant No. 21K05266 to Yukari Sato); Tohoku University Center for Gender Equality Promotion Support Program (TUMUG; grant to Yukari Sato); Platform Project for Supporting Drug Discovery and Life Science Research [Basis for Supporting Innovative Drug Discovery and Life Science Research (BINDS)] from AMED (grant No. JP25am121001).

References

Agirre, J., Atanasova, M., Bagdonas, H., Ballard, C. B., Baslé, A., Beilsten-Edmands, J., Borges, R. J., Brown, D. G., Burgos-Mármol, J. J., Berrisford, J. M., Bond, P. S., Caballero, I., Catapano, L., Chojnowski, G., Cook, A. G., Cowtan, K. D., Croll, T. I., Debreczeni, J. É., Devenish, N. E., Dodson, E. J., Drevon, T. R., Emsley, P., Evans, G., Evans, P. R., Fando, M., Foadi, J., Fuentes-Montero, L., Garman, E. F., Gerstel, M., Gildea, R. J., Hatti, K., Hekkelman, M. L., Heuser, P., Hoh, S. W., Hough, M. A., Jenkins, H. T., Jiménez, E., Joosten, R. P., Keegan, R. M., Keep, N., Krissinel, E. B., Kolenko, P., Kovalevskiy, O., Lamzin, V. S., Lawson, D. M., Lebedev, A. A., Leslie, A. G. W., Lohkamp, B., Long, F., Malý, M., McCoy, A. J., McNicholas, S. J., Medina, A., Millán, C., Murray, J. W., Murshudov, G. N., Nicholls, R. A., Noble, M. E. M., Oeffner, R., Pannu, N. S., Parkhurst, J. M., Pearce, N., Pereira, J., Perrakis, A., Powell, H. R., Read, R. J., Rigden, D. J., Rochira, W., Sammito, M., Sánchez Rodríguez, F., Sheldrick, G. M., Shelley, K. L., Simkovic, F., Simpkin, A. J., Skubak, P., Sobolev, E., Steiner, R. A., Stevenson, K., Tews, I., Thomas, J. M. H., Thorn, A., Valls, J. T., Uski, V., Usón, I., Vagin, A., Velankar, S., Vollmar, M., Walden, H., Waterman, D., Wilson, K. S., Winn, M. D., Winter, G., Wojdyr, M. & Yamashita, K. (2023). *Acta Cryst.* D**79**, 449–461.

Chong, S., Shao, Y., Paulus, H., Benner, J., Perler, F. B. & Xu, M. Q. (1996). *J. Biol. Chem.* **271**, 22159–22168.

Dauter, Z. (2003). *Acta Cryst.* D**59**, 2004–2016.

Dierks, K., Meyer, A., Einspahr, H. & Betzel, C. (2008). *Cryst. Growth Des.* **8**, 1628–1634.

Efremov, R., Moukhametzianov, R., Büldt, G. & Gordeliy, V. (2004). *Biophys. J.* **87**, 3608–3613.

Epps, D. E., Sarver, R. W., Rogers, J. M., Herberg, J. T. & Tomich, P. K. (2001). *Anal. Biochem.* **292**, 40–50.

Ericsson, U. B., Hallberg, B. M., DeTitta, G. T., Dekker, N. & Nordlund, P. (2006). *Anal. Biochem.* **357**, 289–298.

Evans, P. R. (2011). *Acta Cryst.* D**67**, 282–292.

Guo, Q., Huang, B., Cheng, J., Seefelder, M., Engler, T., Pfeifer, G., Oeckl, P., Otto, M., Moser, F., Maurer, M., Pautsch, A., Baumeister, W., Fernández-Busnadiego, R. & Kochanek, S. (2018). *Nature* **555**, 117–120.

Hamdane, D., Lechauve, C., Marden, M. C. & Golinelli-Pimpaneau, B. (2009). *Acta Cryst.* D**65**, 388–392.

Harada, A., Sato, Y., Kamimura, N., Venugopalan, N., Masai, E. & Senda, T. (2016). *Acta Cryst.* F**72**, 897–902.

Heras, B., Edeling, M. A., Byriel, K. A., Jones, A., Raina, S. & Martin, J. L. (2003). *Structure* **11**, 139–145.

Higgins, M. K. & Lea, S. M. (2017). *Curr. Opin. Struct. Biol.* **46**, 95–101.

Hiraki, M., Kato, R., Nagai, M., Satoh, T., Hirano, S., Ihara, K., Kudo, N., Nagae, M., Kobayashi, M., Inoue, M., Uejima, T., Oda, S., Chavas, L. M. G., Akutsu, M., Yamada, Y., Kawasaki, M., Matsugaki, N., Igarashi, N., Suzuki, M. & Wakatsuki, S. (2006). *Acta Cryst.* D**62**, 1058–1065.

Inagaki, E., Takahashi, H., Kuroishi, C. & Tahirov, T. H. (2005). *Acta Cryst.* F**61**, 609–611.

Jancarik, J. & Kim, S.-H. (1991). *J. Appl. Cryst.* **24**, 409–411.

Kabsch, W. (2010). *Acta Cryst.* D**66**, 125–132.

Katsuyama, Y., Sato, Y., Sugai, Y., Higashiyama, Y., Senda, M., Senda, T. & Ohnishi, Y. (2018). *FEBS J.* **285**, 1540–1555.

Kiefersauer, R., Than, M. E., Dobbek, H., Gremer, L., Melero, M., Strobl, S., Dias, J. M., Soulimane, T. & Huber, R. (2000). *J. Appl. Cryst.* **33**, 1223–1230.

Liebschner, D., Afonine, P. V., Baker, M. L., Bunkóczi, G., Chen, V. B., Croll, T. I., Hintze, B., Hung, L.-W., Jain, S., McCoy, A. J., Moriarty, N. W., Oeffner, R. D., Poon, B. K., Prisant, M. G., Read, R. J., Richardson, J. S., Richardson, D. C., Sammito, M. D., Sobolev, O. V., Stockwell, D. H., Terwilliger, T. C., Urzhumtsev, A. G., Videau, L. L., Williams, C. J. & Adams, P. D. (2019). *Acta Cryst.* D**75**, 861–877.

Liu, Q. & Hendrickson, W. A. (2017). *Methods Mol. Biol.* **1607**, 377–399.

Matthews, B. W. (1968). *J. Mol. Biol.* **33**, 491–497.

McPherson, A. & Gavira, J. A. (2014). *Acta Cryst.* F**70**, 2–20.

Nevskaya, N., Tishchenko, S., Gabdoulkhakov, A., Nikonova, E., Nikonov, O., Nikulin, A., Platonova, O., Garber, M., Nikonov, S. & Piendl, W. (2005). *Nucleic Acids Res.* **33**, 478–485.

Niesen, F. H., Berglund, H. & Vedadi, M. (2007). *Nat. Protoc.* **2**, 2212–2221.

Padilla, J. E. & Yeates, T. O. (2003). *Acta Cryst.* D**59**, 1124–1130.

Pantoliano, M. W., Petrella, E. C., Kwasnoski, J. D., Lobanov, V. S., Myslik, J., Graf, E., Carver, T., Asel, E., Springer, B. A., Lane, P. & Salemme, F. R. (2001). *SLAS Discov.* **6**, 429–440.

Parsons, S. (2003). *Acta Cryst.* D**59**, 1995–2003.

Phillips, K. & de la Peña, A. H. (2011). *Mol. Biol.* **94**, 10.

Poklar, N., Lah, J., Salobir, M., Maček, P. & Vesnaver, G. (1997). *Biochemistry* **36**, 14345–14352.
Ray-Gallet, D., Ricketts, M. D., Sato, Y., Gupta, K., Boyarchuk, E., Senda, T., Marmorstein, R. & Almouzni, G. (2018). *Nat. Commun.* **9**, 3103.
Ray-Gallet, D., Woolfe, A., Vassias, I., Pellentz, C., Lacoste, N., Puri, A., Schultz, D. C., Pchelintsev, N. A., Adams, P. D., Jansen, L. E. & Almouzni, G. (2011). *Mol. Cell* **44**, 928–941.
Ristic, M., Rosa, N., Seabrook, S. A. & Newman, J. (2015). *Acta Cryst.* F**71**, 1359–1364.
Santos, S. P., Bandeiras, T. M., Pinto, A. F., Teixeira, M., Carrondo, M. A. & Romão, C. V. (2012). *Protein Expr. Purif.* **81**, 193–200.
Sato, Y., Natsume, R., Tsuda, M., Damborsky, J., Nagata, Y. & Senda, T. (2007). *Acta Cryst.* F**63**, 294–296.
Senda, M., Hayashi, T., Hatakeyama, M., Takeuchi, K., Sasaki, A. T. & Senda, T. (2016). *Cryst. Growth Des.* **16**, 1565–1571.
Senda, M., Muto, S., Horikoshi, M. & Senda, T. (2008). *Acta Cryst.* F**64**, 960–965.
Senda, M. & Senda, T. (2016). *Advanced methods in structural biology*, edited by T. Senda & K. Maenaka, pp. 139–151. Tokyo: Springer Japan.
Sharma, M. & Kumar, V. (2019). *Int. J. Biol. Macromol.* **140**, 1315–1325.
Shoemaker, S. C. & Ando, N. (2018). *Biochemistry* **57**, 277–285.
Skagseth, S., Christopeit, T., Akhter, S., Bayer, A., Samuelsen, Ø. & Leiros, H.-K. S. (2017). *Antimicrob. Agents Chemother.* **61**, e02602-16.
Slabinski, L., Jaroszewski, L., Rychlewski, L., Wilson, I. A., Lesley, S. A. & Godzik, A. (2007). *Bioinformatics* **23**, 3403–3405.
Stura, E. A. & Wilson, I. A. (1991). *J. Cryst. Growth* **110**, 270–282.
Sugai, Y., Katsuyama, Y. & Ohnishi, Y. (2016). *Nat. Chem. Biol.* **12**, 73–75.
Tagami, H., Ray-Gallet, D., Almouzni, G. & Nakatani, Y. (2004). *Cell* **116**, 51–61.
Thompson, M. C. (2017). *Methods Mol. Biol.* **1607**, 185–217.
Vedadi, M., Arrowsmith, C. H., Allali-Hassani, A., Senisterra, G. & Wasney, G. A. (2010). *J. Struct. Biol.* **172**, 107–119.
Vedadi, M., Niesen, F. H., Allali-Hassani, A., Fedorov, O. Y., Finerty, P. J., Wasney, G. A., Yeung, R., Arrowsmith, C., Ball, L. J., Berglund, H., Hui, R., Marsden, B. D., Nordlund, P., Sundstrom, M., Weigelt, J. & Edwards, A. M. (2006). *Proc. Natl Acad. Sci. USA* **103**, 15835–15840.
wwwPDB Consortium (2024). *Nucleic Acids Res.* **52**, D456–D465.
Yeates, T. O. & Fam, B. C. (1999). *Structure* **7**, R25–R29.
Zhang, Z., Sauter, N. K., van den Bedem, H., Snell, G. & Deacon, A. M. (2006). *J. Appl. Cryst.* **39**, 112–119.